P528 #7: Testing the SM

David Morrissey
March 16, 2021

The Standard Model (SM) was built up over many years with contributions from a very large number of people. An important part of this process was the interplay between experiment and theory. Experimental discoveries were synthesized and explained using theoretical models, which were then tested and applied to guide new experimental explorations.

In these notes we describe how the SM has been tested experimentally. The key idea is that the theory predicts correlations between a large number of physical observables. This implies that observables can be predicted in terms of other observables without reference to the underlying parameters of the Lagrangian, and this provides an unambiguous test of the theory.

For now, we will focus on the electroweak and Higgs sectors of the SM. Some additional theoretical technology is needed to discuss the strong sector of the SM in detail, and we will come back to it later in the course.

1 Precision Electroweak Tests of the SM

The electroweak sector of the Standard Model (SM) has been tested extensively in both high-energy particle collisions and lower-energy precision probes. These tests have given us confidence that a $SU(2)_L \times U(1)_Y$ gauge invariance underlies both the electromagnetic and weak forces. In this section we discuss how to connect the SM theory to experimental observables.

1.1 Tree Level Analysis

Recall from our previous investigation of the SM that the electroweak sector is completely characterized by three independent parameters, which can be chosen to be $\{e, s_W, v\}$. Once we fix the values of these parameters, by making three independent experimental measurements, we can predict all the other (tree-level) electroweak observables in the SM [1, 2]. It is convenient to choose these three "input" observables to be α, G_F, and m_Z since they are among the best-measured quantities in the electroweak part of the SM.

The electromagnetic coupling α_{em} is determined at low energy from the anomalous magnetic moment of the electron, and is then extrapolated up to a value relevant for physics at energies close to m_Z. The current status is [3, 4]

$$
\begin{aligned}
\alpha(m_Z) \ &:= \ \frac{e^2}{4\pi} \ = \ \frac{g^2 s_W^2}{4\pi} \\
&= \ (127.95 \pm 0.02)^{-1} \ .
\end{aligned}
\tag{1}
$$

Muon decays are used to extract the Fermi constant G_F, which is given by

$$G_F := \frac{1}{2\sqrt{2}\,v^2} \tag{2}$$
$$= (1.1663787 \pm 0.00000006) \times 10^{-5} \text{ GeV}^{-2} .$$

The mass of the Z^0 is deduced from the energy dependence of the $e^+e^- \to f\bar{f}$ cross section for $\sqrt{s} \sim m_Z$:

$$m_Z = \frac{e}{\sqrt{2}\,s_W c_W}\,v \tag{3}$$
$$= (91.188 \pm 0.002) \text{ GeV} .$$

It is straightforward to solve for e, s_W, and v from these expressions:

$$e = \sqrt{4\pi\,\alpha} \simeq 0.313 \tag{4}$$
$$v = 1/\sqrt{2\sqrt{2}G_F} \simeq 174 \text{ GeV} \tag{5}$$
$$s_W^2 = \frac{1}{2} - \frac{1}{2}\sqrt{1 - 4\pi\alpha/\sqrt{2}G_F m_Z^2} \simeq 0.234 . \tag{6}$$

Note that we take s_W to be the positive square root, with c_W positive as well.

Having fixed the input values of the Lagrangian, we can now go on to compute any other electroweak observable we would like. The most useful of these for testing the SM are usually the so-called *Z-pole* observables, corresponding to processes of the form $e^+e^- \to f\bar{f}$ at centre-of-mass (CM) energies near the Z^0 mass, $s = (p_{e^-} + p_{e^+})^2 \simeq m_Z^2$. In this regime, the dominant contribution to the cross section comes from the diagram with a Z^0 in the s-channel.[1] The dominance of this diagram comes about because of the form of the Z^0 propagator denominator appearing in the amplitude:

$$\mathcal{M} \propto \frac{1}{p^2 - m_Z^2} . \tag{7}$$

This evidently has a pole at $p^2 = s = m_Z^2$.

The blowup here is not physical, however. Adding quantum corrections to the propagator, primarily in the form of fermion loops, the propagator denominator acquires an imaginary piece that is approximated well by [5, 6]

$$\frac{1}{p^2 - m_Z^2} \to \frac{1}{p^2 - m_Z^2 + i\sqrt{p^2}\,\Gamma_Z}, \tag{8}$$

where Γ_Z is the *total* decay width of the Z^0 into all possible final states. The new contribution is imaginary, meaning that it is an absorptive effect in the propagation of the Z^0 corresponding to the loss of propagation probability amplitude due to its finite lifetime ($\tau_Z = 1/\Gamma_Z$)

---

[1]For $f \neq e$ the other tree-level diagram has an s-channel photon. There are additional t-channel photon and Z^0 diagrams for $f = e$.
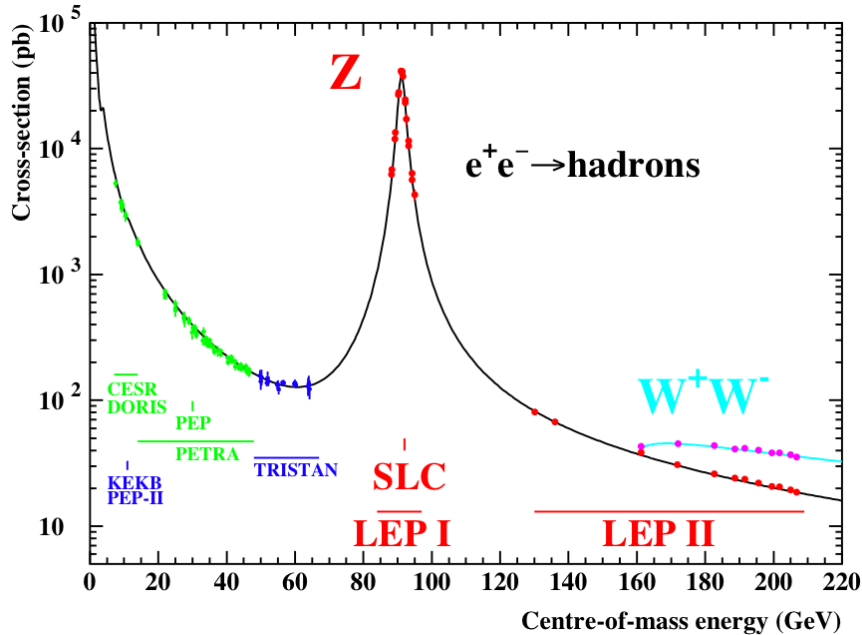
Figure 1: Cross section for $e^+e^- \to$ hadrons (and W^+W^-) at various energies.

to decay into other particles. Numerically, $\Gamma_Z \ll m_Z$, implying that the propagator still receives a large enhancement for p^2 close to m_Z^2.

The master equation for computing Z-pole electroweak observables is the differential cross-section for $e^+e^- \to f\bar{f}$ via the Z^0 in the CM frame, and is given by (neglecting light fermion masses)

$$
\begin{aligned}
\frac{d\sigma}{d\cos\theta} =\ & \frac{N_c}{128\pi} \frac{s}{(s - m_Z^2)^2 + s\Gamma_Z^2} \\
& \left[(|a_{LL}|^2 + |a_{RR}|^2 + |a_{LR}|^2 + |a_{RL}|^2)(1 + \cos^2\theta) \right. \\
& \left. + (|a_{LL}|^2 + |a_{RR}|^2 - |a_{LR}|^2 - |a_{RL}|^2)(2\cos\theta) \right] \ ,
\end{aligned}
\tag{9}
$$

where $\cos\theta$ is the scattering angle of the f fermion relative to the electron beam, N_c is the number of colours of the fermion, and the coefficients are

$$
a_{AB} = g_A^e g_B^f \ ,
\tag{10}
$$

with A, $B = L$, R. Recall that $g_A^f = (e/s_W c_W)(t^3 - Q s_W^2)$.

An obvious first thing to look at is the energy dependence of the cross-section for $\sqrt{s}$ close to m_Z. The LEP-I (CERN) and SLC (SLAC) experiments did just this and found a clear mass peak, as shown in Fig. 1. Based on the location and shape of the peak, it is possible to extract m_Z and Γ_Z. The value of m_Z is used as an input observable, but [3]

$$
\Gamma_Z = (2.495 \pm 0.002) \text{ GeV}
\tag{11}
$$

is an independent output observable whose value we can also be computed in terms of the inputs.

3

After figuring out the location of the Z pole, the LEP-I and SLC (and SLD) experiments ran primarily on the pole with $\sqrt{s} = m_Z$, or at least as close to it as they could get. In this situation, we can think of $e^+e^- \to f\bar{f}$ process as $e^+e^- \to Z^0$ followed by $Z^0 \to f\bar{f}$. The relative cross-sections for different fermion final states are then proportional to the partial decay widths of the Z^0 into these final states. This allows for the extraction of the branching fractions (or ratios) of the Z^0,

$$\mathrm{BR}_f \; := \; \Gamma(Z \to f\bar{f})/\Gamma_Z \; := \; \Gamma_f/\Gamma_Z \; . \tag{12}$$

These can again be compared to the values predicted by the SM. Sometimes you will see various R_f quantities defined according to

$$R_\ell = \Gamma_{had}/\Gamma_\ell \;\; (\ell = e, \mu, \tau) \;, \qquad R_b = \Gamma_b/\Gamma_{had} \;, \qquad R_c \equiv \Gamma_c/\Gamma_{had} \;, \tag{13}$$

where Γ_{had} the decay width into all the kinematically accessible quarks.

Unlike all the other Z^0 decay channels, the neutrino final states are not seen directly. Instead one can deduce the total *invisible* partial width of the Z^0 by using

$$\Gamma_{inv} = \Gamma_Z - \Gamma_e - \Gamma_\mu - \Gamma_\tau - \Gamma_{had} \; . \tag{14}$$

Comparing Γ_{inv} to the SM prediction for neutrinos, the data only matches what is seen if there are three (active) neutrino species. The current experimental uncertainty in Γ_{inv} implies that any additional (non-SM neutrino) invisible Z^0 decay channels must have a total width less than $\Delta\Gamma_{inv} \lesssim 2$ MeV.

Besides just branching fractions and overall cross-sections, there is additional information to be had in angular distributions and spins. The left-right asymmetry A_f is defined to be

$$A_f \equiv \left[\Gamma(Z \to f_L\bar{f}_R) - \Gamma(Z \to f_R\bar{f}_L)\right]/\Gamma(Z \to f\bar{f}) \; . \tag{15}$$

Here, $\bar{f}_R$ is the right-handed anti-fermion conjugate of f_L, and could more properly be written as $\overline{(f_L)}$.[2] It is not hard to show that

$$A_f = \frac{(g_L^f)^2 - (g_R^f)^2}{(g_L^f)^2 + (g_R^f)^2} \; . \tag{16}$$

These left-right asymmetries can be measured using polarized electron beams at the Z pole, which was done at the SLAC SLD experiments. Note that sometimes one also sees $A_f = A_{LR}^f$.

The forward-backward asymmetry in $e^+e^- \to f\bar{f}$ is defined by

$$A_{FB}^f \; := \; \frac{\left(\int_0^1 - \int_{-1}^0\right) d(\cos\theta) \, \frac{d\sigma(e^+e^- \to f\bar{f})}{d(\cos\theta)}}{\left(\int_0^1 + \int_{-1}^0\right) d(\cos\theta) \, \frac{d\sigma(e^+e^- \to f\bar{f})}{d(\cos\theta)}} \; . \tag{17}$$

This quantity is a function of the CM energy $\sqrt{s}$, but it is usually quoted for $\sqrt{s} = m_Z$. On the Z pole, one can show that

$$A_{FB}^f = \frac{3}{4}A_e A_f \; . \tag{18}$$

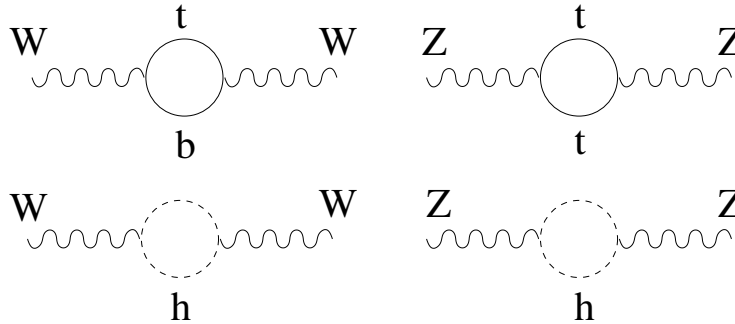[2] Recall that the conjugate of a 2-component LH fermion is a RH 2-component fermion.

Figure 2: Some of the diagrams involving the top quark and Higgs boson giving rise to oblique corrections to the weak vector boson propagators.

In addition to these primarily Z-pole observables, there are also some very good tests of the electroweak structure of the SM at both lower and higher energies. At lower energies, precision measurements neutrino cross-sections, atomic parity violation, and the determination of the τ lifetime are especially important. Higher energy colliders such as the Tevatron and the LHC have measured m_W very precisely [7, 8]:

$$m_W = (80.387 \pm 0.019) \text{ GeV} \tag{19}$$

These colliders have also measured rates of single and double W and Z production, which can again be compared with the predictions of the SM.

1.2 Beyond Tree Level

The current set of experimental tests of the electroweak sector of the SM are so good that loop corrections must be included in the theoretical predictions to achieve the same level of precision as the data. However, adding loops also introduces a number of complications in addition to the direct technical challenge of computing loop diagrams. These include renormalization, scale dependence, scheme dependence, and effects related to the non-electroweak parts of the SM theory.

Many loops contain formally divergent integrals. These typically arise from integrating over all possible momenta of intermediate states in loops, with the divergences coming specifically from the limit of these momenta becoming very large. Dealing with such infinities will be discussed later in the course, but for now let us assume that we can find a way to modify the SM at unobservably high energies such that the would-be divergences become finite. The main result for the SM, and more generally for theories that are *renormalizable*, is that the explicit dependence on this modification (at energies well below where it becomes important) disappears completely when physical observables are written in terms of a finite set of basis input observables. This is precisely the approach we took above.

Loops also connect the electroweak parameters to other parameters in the theory. The most important loops are typically the so-called *oblique* corrections, corresponding to loops in the propagators of the electroweak vector bosons. For example, diagrams involving top quarks or Higgs bosons modify the tree-level relationship between the observable Z^0 and
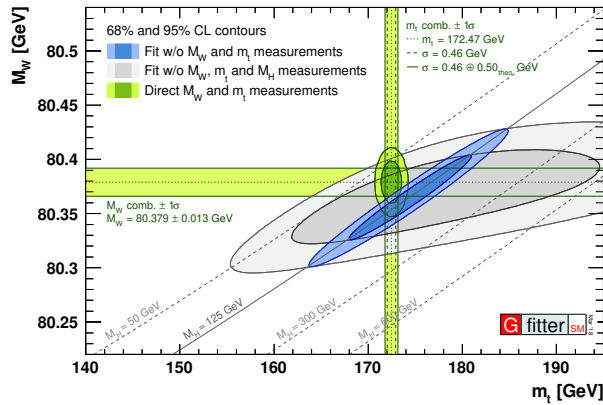
Figure 3: Dependence of the fit to precision electroweak observables as function of the top, W, and Higgs boson masses. Also shown are the direct measurements of the top and W masses.

$W^{\pm}$ masses, making their values dependent on the top quark and Higgs masses. Some of these diagrams are illustrated in Fig. 2. In fact, collecting the effects of the top and Higgs on various precision electroweak observables, impressively good predictions can be made for their masses. An illustration of this dependence is shown in Fig. 3, from Refs. [9, 10].

1.3 The Current Status of the EW Sector of the SM

Comparing the theoretical predictions of the SM to experimental measurements, the theory does extremely well in nearly every regard. As such, the SM really does appear to be the correct theory of nature at energies up to at least a few hundreds of GeV.

The results of a recent global fit of the SM theory to precision electroweak data are shown in the panel Fig. 4 [10]. In this figure, the bars show the difference between the best-fit theory predictions of the SM and the experimentally measured values for a number of mostly Z-pole SM observables, in units of the experimental uncertainty. While there are some deviations, they are consistent with statistical fluctuations in the experiments.

The SM has also been tested stringently at energies well above the Z-pole at the LHC. In the right panel of Fig. 4, we show the values of various electroweak vector boson (and top quark) production rates measured by the ATLAS experiment at the LHC [11, 12]. An impressive agreement between the SM theory and experiment is found over many orders of magnitude.

2 Higgs Physics

The last particle predicted by the SM to be found was the Higgs boson. The discovery of a new particle of mass $m \simeq 125$ GeV with the right properties to be the SM Higgs was
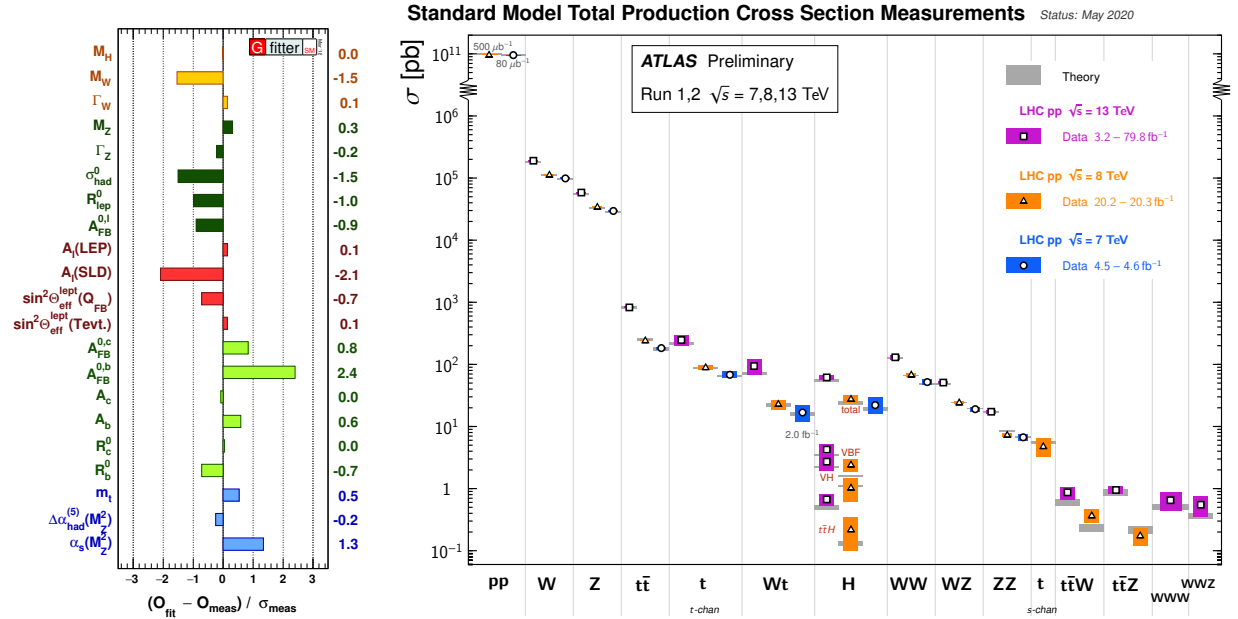
Figure 4: *Left:* Observed values of various electroweak observables compared to the best-fit predictions of the SM, from Ref. [10]. *Right:* Production cross sections for the electroweak vector bosons measured at the LHC by the ATLAS experiment compared to theory [11].

announced on July 4, 2012.[3] In the years since, many further measurements have confirmed that this new particle has the properties expected of the SM Higgs, giving us confidence that it is the genuine article. In this section, we discuss how the SM Higgs boson decays, how it can be produced in high-energy collisions, and how these properties were used to discover it. More detailed reviews can be found in Refs. [13, 14, 15, 16].

2.1   Higgs Decays

Recall that the Higgs boson couples to other particles in the SM proportionally to their masses [17]. This implies that it decays most often to the heaviest particles it can. For a SM Higgs with mass $m_h = 125$ GeV, the leading decay mode is $h \to b\bar{b}$. After this, the most important decays involve WW^*, gg, ZZ^*, $\tau\bar{\tau}$, and $c\bar{c}$.

The leading-order Higgs decay width to fermion pairs $h \to f\bar{f}$ is

$$\Gamma(h \to f\bar{f}) = \frac{N_c}{8\pi} \left(\frac{m_f}{\sqrt{2}\,v} \right)^2 m_h \left[1 - \left(\frac{2m_f}{m_h} \right)^2 \right]^{3/2} , \qquad (20)$$

where m_f is the fermion mass and N_c is the number of colours of the fermion, equal to three for quarks and one for leptons. This expression shows the explicit dependence of the decay
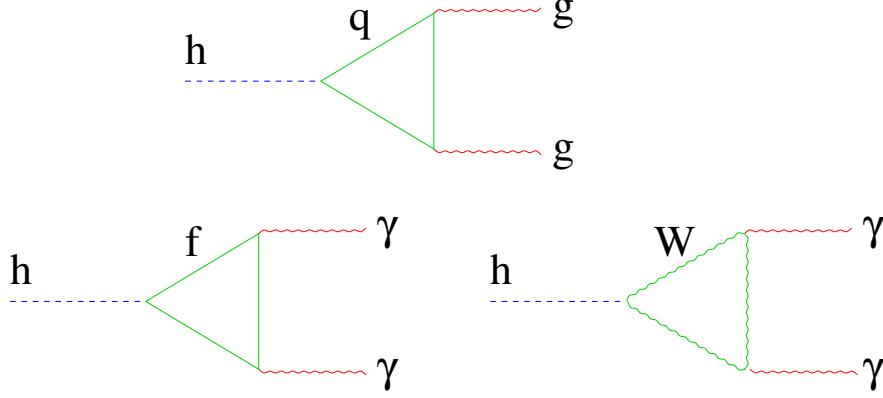
---

[3] *Higgsdependence Day!*

Figure 5: Loop diagrams contribution to $h \to gg$ (*top*) and $h \to \gamma\gamma$ (*bottom*).

width on the mass of the final-state fermion, corresponding to the strength of the Higgs coupling.

If the Higgs were heavier, it would also be able to decay to a pair of on-shell weak vector bosons. The corresponding widths at leading order are

$$\Gamma(h \to VV) = \frac{N_V}{64\pi} \frac{m_h^3}{v^2} \left[1 - \left(\frac{2m_V}{m_h} \right)^2 \right]^{1/2} \left[1 - 4 \left(\frac{m_V}{m_h} \right)^2 + 12 \left(\frac{m_V}{m_h} \right)^4 \right] , \qquad (21)$$

where $N_V = 2, 1$ for $V = W, Z$. Note that these 2-body decays do not occur in the SM for $m_h = 125$ GeV due to kinematics. However, the 3-body decays $h \to VV^*$ is significant, where V^* represents an intermediate off-shell weak vector boson in the diagram that connects to a pair of light SM fermions. The corresponding 3-body rates are suppressed by factors of about $g^2/(4\pi)^2$ relative to the widths for the 2-body mode.

The Higgs boson can also decay to a pair of gluons or photons through loop effects. For the gluon mode, diagrams of the form shown in Fig. 5 lead to a one-loop width of

$$\Gamma(h \to gg) = \frac{\alpha_s^2}{128\pi^3} \frac{m_h^3}{v^2} \left| \frac{3}{4} \sum_q A_{1/2}(\tau_q) \right|^2 , \qquad (22)$$

where the sum runs over quarks, $\tau_i = (m_h/2m_i)^2$, and

$$A_{1/2}(\tau) = \frac{2}{\tau^2} \left[\tau + (\tau - 1)f(\tau) \right] , \qquad (23)$$

with

$$f(\tau) = \begin{cases} [\sin^{-1}(\sqrt{\tau})]^2 & ; \quad \tau \leq 1 \\ -\frac{1}{4} \left[\ln \left(\frac{1+\sqrt{1-\tau^{-1}}}{1-\sqrt{1-\tau^{-1}}} \right) + i\pi \right]^2 & ; \quad \tau > 1 \end{cases} . \qquad (24)$$

While the loop function $A_{1/2}(\tau)$ is complicated, it has simple limits for large or small τ,

$$A_{1/2}(\tau) \rightarrow \begin{cases} 4/3 & ; \quad \tau \ll 1 \\ -\ln(4\tau)/2\tau & ; \quad \tau \gg 1 \end{cases} . \tag{25}$$

These limits imply that the $h \rightarrow gg$ decay width is dominated by the top quark loop for $m_h = 125$ GeV. In the limit of $m_t \gg m_h$, corresponding to $A_{1/2}(\tau_t) \rightarrow 4/3$, it is often useful to think about the top loop as generating a low-energy effective operator of the form [18]

$$\mathscr{L}_{eff} \supset \frac{\alpha_s}{24\pi} \frac{y_t^2}{m_t^2} H^\dagger H\, G^a_{\mu\nu} G^{a\,\mu\nu} . \tag{26}$$

This is the leading gauge-invariant effective operator that connects the Higgs to the gluon.

Decays of the Higgs to pairs of photons are rare, but they played a leading role in the discovery of the Higgs. The decay arises from loop diagrams involving charged fermions and W bosons, as shown in Fig. 5. At one-loop order, the width is

$$\Gamma(h \rightarrow \gamma\gamma) = \frac{\alpha^2}{512\pi^3} \frac{m_h^3}{v^2} \left| A_1(\tau_W) + \sum_f N_c Q_f^2 A_{1/2}(\tau_f) \right|^2 , \tag{27}$$

where $\tau_i = (m_h/2m_i)^2$, Q_f is the electromagnetic charge of fermion f, $A_{1/2}(\tau)$ is given in Eq. (23), and

$$A_1(\tau) = -\frac{1}{\tau^2} \left[2\tau^2 + 3\tau + 3(2\tau - 1)f(\tau) \right] , \tag{28}$$

with $f(\tau)$ given in Eq. (24). We have $A_1 \sim \ln(\tau)/\tau$ for $\tau \gg 1$, while $A_1(\tau) \rightarrow -7$ for $\tau \ll 1$. The most important contributions to the diphoton width are W loops, followed by the top loop. As for the gluon decay mode, it is often useful to think of the W and t loops as generating a gauge-invariant effective operator of the form $H^\dagger H\, F_{\mu\nu} F^{\mu\nu}$ [18].

Summing up all the possible decay modes of the SM Higgs, the total decay width is predicted to be [19, 20]

$$\Gamma_{tot} = 4.1 \pm 0.2 \text{ MeV} . \tag{29}$$

This is much smaller than the mass of the Higgs boson due to its very small couplings to the particles it can decay to. Recall as well that the *branching ratio* for the i-th decay mode is defined to be $\text{BR}_i = \Gamma_i/\Gamma_h$. The branching ratio for mode i can be understood as the probability for the Higgs to decay in that channel. In Fig. 6 we show the predicted SM Higgs branching ratios as a function of the Higgs mass. As expected, the $h \rightarrow b\bar{b}$ dominates, with the other fractions corresponding to the relative couplings of the final states to the Higgs.

2.2 Higgs Production at Colliders

Producing Higgs bosons at colliders depends on what kinds of particles are smashed together. Recent high-energy colliders have used beams of protons, antiprotons, electrons, and
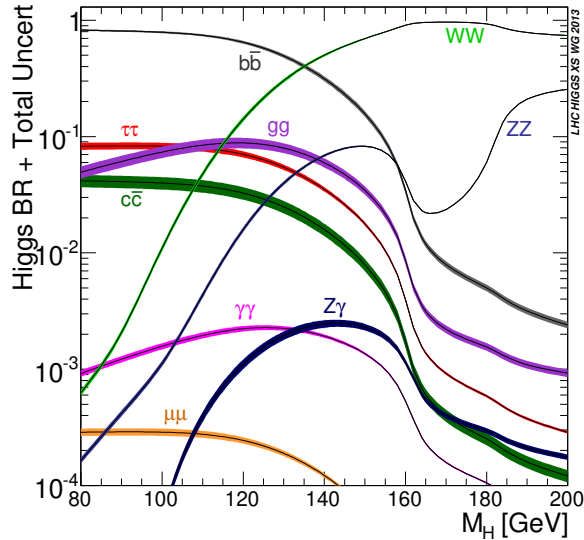
Figure 6: Branching fractions of the SM Higgs boson as a function of the Higgs mass for the most important decay channels.

antielectrons. Since these consist of light quarks or leptons, creating Higgs bosons directly at these colliders is a challenge.

The most useful Higgs production mode at electron-positron colliders is $e^+e^- \to Z^* \to Zh$. In this process, sometimes called *higgstrahlung*, a virtual Z boson is created in the s-channel, which then splits into on-shell Z and h particles. The couplings involved are all electroweak, and the net production rate is similar to WZ or ZZ. However, the minimum collision energy is $\sqrt{s} = (m_Z + m_h) \simeq 216$ GeV, and this is larger than has ever occurred in stable laboratory e^+e^- collisions.

Higher energies can be achieved in proton-proton (or proton-antiproton) collisions. Note that high-energy proton collisions can be thought of as collisions of the underlying quarks and gluons that make them up. Diagrams for the most important Higgs production channels for LHC pp collisions are shown in the left panel of Fig. 7. The leading production channel is *gluon fusion*, corresponding to $gg \to h$ through the same top loop diagram that leads to $h \to gg$ decays and shown in the top diagram of the left panel of Fig. 7. The next largest mode is vector boson fusion (VBF), in which a pair of W or Z bosons join to make a Higgs, as shown in the second diagram on the left in Fig. 7. In VBF, the Higgs boson is accompanied by a pair of high-energy quarks with distinctive kinematics that can be used to identify this channel. The bottom two diagrams in Fig. 7 correspond to vector-boson associated production (Vh, where $V = W, Z$), and $t\bar{t}h$ associated production. In both cases, the Higgs is radiated off a massive SM particle. The right panel of Fig. 7 shows the relative sizes of these various production modes at the LHC for a collision energy of $\sqrt{s} = 13$ TeV. Note that $pp \to H$ corresponds mainly gluon fusion, qqH refers to VBF, WH and ZH are vector-boson associated production, and $t\bar{t}h$ is self-evident.
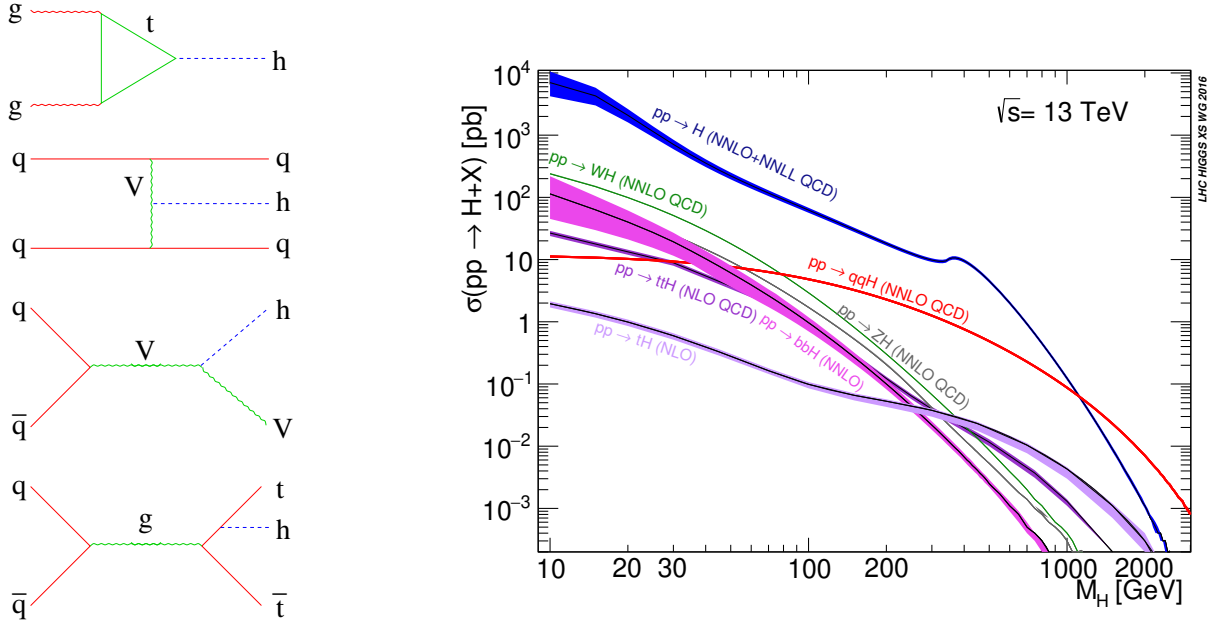
10

Figure 7: *Left:* Diagrams contributing to Higgs production through gluon fusion, vector boson fusion, Vh associated production, and $t\bar{t}h$. *Right:* Production cross sections for these modes at the LHC with $\sqrt{s} = 13$ TeV.

2.3 Higgs Searches, Discovery, and Tests

Despite being first proposed in 1964 [21, 22, 23, 24], it took until 2012 to discover the Higgs boson. This was not for lack of trying. Experiments had been searching for the Higgs for nearly forty years, but it took the full power of the LHC collider to find it.

Even before the start of the LHC, precision electroweak measurements gave very strong indirect evidence for the Higgs. Recall that the Higgs mass enters into loop corrections to electroweak observables. To obtain a viable fit to these observables using the SM theory, it was necessary to assume the existence of the Higgs and include its effects in the theoretical predictions. Furthermore, the data was only consistent with the SM for a Higgs mass below about $m_h \lesssim 160$ GeV [10]. The dependence of the fit on m_h can be seen in Fig. 3.

Before its discovery, the mass of the Higgs was also bounded from below by searches at the LEP II experiment. This was an e^+e^- collider (in the same tunnel that currently houses the LHC) with centre-of-mass (CM) collision energies up to $\sqrt{s} \simeq 208$ GeV. The most efficient search channel at LEP II was $e^+e^- \to Z^* \to Zh$, followed by $h \to b\bar{b}$. Their maximum collision energy turned out to be just below what was needed to produce the Higgs, but they were able to place a stringent lower bound on the mass of $m_h > 114.4$ GeV [25]. These limits were further improved by searches at the Tevatron, a $p\bar{p}$ collider running at CM energies up to $\sqrt{s} = 1.96$ TeV [26].

The LHC is a pp collider that ran at CM energies of $\sqrt{s} = 7, 8$ TeV in its initial science run. At these energies, the dominant Higgs production and decay channels are
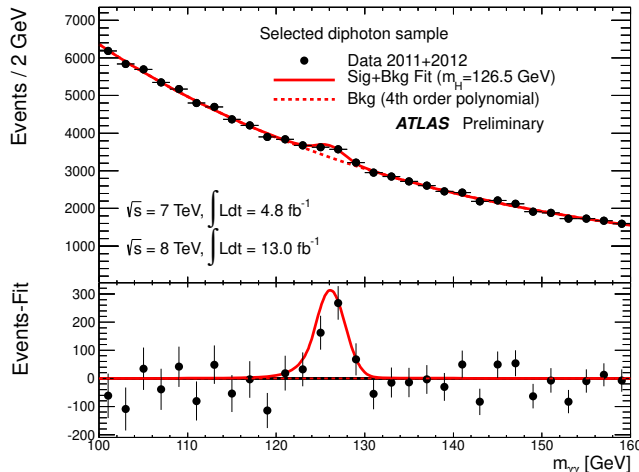
Figure 8: Diphoton invariant masses measured by the ATLAS experiment at the LHC. The bump at $m_{\gamma\gamma} \simeq 125$ GeV is consistent with a SM Higgs boson of that mass [27].

gluon fusion followed by $h \to b\bar{b}$. Unfortunately, this signal process is completely swamped by $b\bar{b}$ background events from QCD processes that do not involve the Higgs. Instead, the most important channel for the initial Higgs discovery was inclusive Higgs production (*i.e.* all possible channels) followed by decays to photon pairs, $h \to \gamma\gamma$. While this decay mode is rare, with $BR(h \to \gamma\gamma) \simeq 0.002$, it is relatively easy to identify in the LHC detectors and it has a relatively small non-Higgs background. These decays can also be identified by combining the measured 4-momenta $p_{1,2}$ of the photons into an *invariant mass*,

$$m_{\gamma\gamma} = \sqrt{(p_1 + p_2)^2} \; . \tag{30}$$

Applying energy-momentum conservation, it is not hard to check that $m_{\gamma\gamma} \simeq m_h$ for a pair of photons from a decaying Higgs boson. In contrast, the diphoton invariant mass distribution from background events falls smoothly. Both features were seen in the data, Fig. 8 [27]. A second important contribution to the discovery was obtained from the $h \to ZZ^*$ decay channel, with each Z decaying to a pair of leptons. In this case, the 4-lepton invariant mass is expected to reconstruct the Higgs mass.

Following the initial discovery, the Higgs boson has been studied in a number of other production channels and decay modes. So far, all the data is consistent with the predictions of the SM [27, 28]. Making a set of fairly mild assumptions (that are consistent with a SM Higgs), the production rates and couplings of the Higgs to many other SM particles can be extracted from the experimental data [27, 28]. The production rates in various channels match the predictions of the SM, and couplings follow the particle masses as expected for the SM. Results from the ATLAS experiment at the LHC exhibiting these features are shown in Fig. 9 [27]. Despite these successes of the SM Higgs description, a great deal of further study is needed to test the Higgs sector thoroughly.
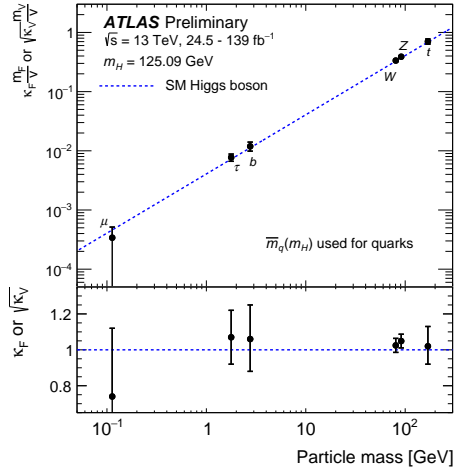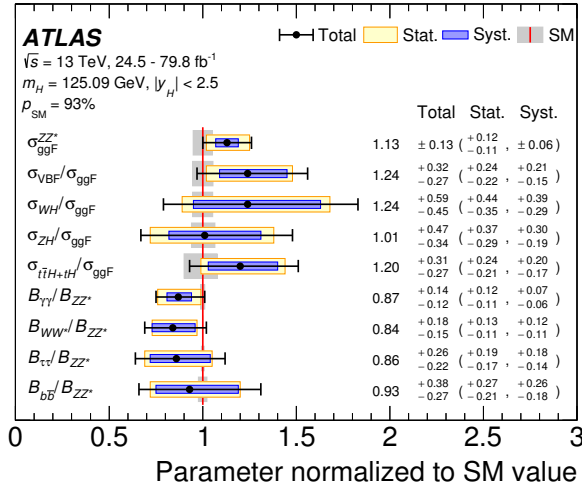
Figure 9: *Left:* Higgs production rates measured by the ATLAS experiment at the LHC in a number of production channels. *Right:* Higgs couplings to other SM particles derived from the data and plotted in relation to the particle masses. Both figures are from Ref. [27].

References

[1] K. Matchev, "TASI lectures on precision electroweak physics," [hep-ph/0402031].

[2] J. D. Wells, "TASI lecture notes: Introduction to precision electroweak analysis," [hep-ph/0512342].

[3] C. Patrignani *et al.* [Particle Data Group], "Review of Particle Physics," Chin. Phys. C **40**, no. 10, 100001 (2016).
See also: http://www-pdg.lbl.gov/

[4] J. Alcaraz [ALEPH and CDF and D0 and DELPHI and L3 and OPAL and SLD Collaboration], "Precision Electroweak Measurements and Constraints on the Standard Model," [arXiv:0911.2604 [hep-ex]].
See also: http://lepewwg.web.cern.ch/LEPEWWG/

[5] M. E. Peskin and D. V. Schroeder, "An Introduction To Quantum Field Theory," *Reading, USA: Addison-Wesley (1995) 842 p*

[6] C. P. Burgess and G. D. Moore, "The standard model: A primer," *Cambridge, UK: Cambridge Univ. Pr. (2007) 542 p*

[7] T. A. Aaltonen *et al.* [CDF Collaboration], "Precise measurement of the W -boson mass with the Collider Detector at Fermilab," Phys. Rev. D **89**, no. 7, 072003 (2014) doi:10.1103/PhysRevD.89.072003 [arXiv:1311.0894 [hep-ex]].

[8] M. Aaboud *et al.* [ATLAS Collaboration], "Measurement of the W-boson mass in pp collisions at $\sqrt{s} = 7$ TeV with the ATLAS detector," arXiv:1701.07240 [hep-ex].

[9] M. Baak *et al.* [Gfitter Group], "The global electroweak fit at NNLO and prospects for the LHC and ILC," Eur. Phys. J. C **74**, 3046 (2014) [arXiv:1407.3792 [hep-ph]]. http://project-gfitter.web.cern.ch/project-gfitter/

[10] GFITTER Group, "A Generic Fitter Project for HEP Model Testing," http://project-gfitter.web.cern.ch/project-gfitter/Standard_Model/

[11] ATLAS Collaboration, "Standard Model Public Results," https://twiki.cern.ch/twiki/bin/view/AtlasPublic/StandardModelPublicResults

[12] CMS Collaboration, "Standard Model Public Results," https://twiki.cern.ch/twiki/bin/view/CMSPublic/PhysicsResultsSMP

[13] J. F. Gunion, H. E. Haber, G. L. Kane and S. Dawson, "The Higgs Hunter's Guide," Front. Phys. **80**, 1 (2000).

[14] M. Carena and H. E. Haber, "Higgs boson theory and phenomenology," Prog. Part. Nucl. Phys. **50**, 63 (2003) doi:10.1016/S0146-6410(02)00177-1 [hep-ph/0208209].

[15] A. Djouadi, "The Anatomy of electro-weak symmetry breaking. I: The Higgs boson in the standard model," Phys. Rept. **457**, 1 (2008) doi:10.1016/j.physrep.2007.10.004 [hep-ph/0503172].

[16] M. Spira, "Higgs Boson Production and Decay at Hadron Colliders," arXiv:1612.07651 [hep-ph].

[17] D. E. Morrissey, "PHYS 528 Notes #5," http://trshare.triumf.ca/ dmorri/Teaching/PHYS528-2017/notes-05.pdf

[18] M. A. Shifman, A. I. Vainshtein, M. B. Voloshin and V. I. Zakharov, Sov. J. Nucl. Phys. **30**, 711 (1979) [Yad. Fiz. **30**, 1368 (1979)].

[19] D. de Florian *et al.* [LHC Higgs Cross Section Working Group], "Handbook of LHC Higgs Cross Sections: 4. Deciphering the Nature of the Higgs Sector," arXiv:1610.07922 [hep-ph].

[20] LHC Higgs Cross Section Working Group, https://twiki.cern.ch/twiki/bin/view/LHCPhysics/LHCHXSWG

[21] P. W. Higgs, "Broken symmetries, massless particles and gauge fields," Phys. Lett. **12**, 132 (1964).

[22] F. Englert and R. Brout, "Broken Symmetry and the Mass of Gauge Vector Mesons," Phys. Rev. Lett. **13**, 321 (1964).

[23] P. W. Higgs, "Broken Symmetries and the Masses of Gauge Bosons," Phys. Rev. Lett. **13**, 508 (1964).

[24] G. S. Guralnik, C. R. Hagen and T. W. B. Kibble, "Global Conservation Laws and Massless Particles," Phys. Rev. Lett. **13**, 585 (1964).

[25] R. Barate *et al.* [ALEPH and DELPHI and L3 and OPAL Collaborations and LEP Working Group for Higgs boson searches], "Search for the standard model Higgs boson at LEP," Phys. Lett. B **565**, 61 (2003) [hep-ex/0306033].

[26] T. Aaltonen *et al.* [CDF and D0 Collaborations], "Higgs Boson Studies at the Tevatron," Phys. Rev. D **88**, no. 5, 052014 (2013) [arXiv:1303.6346 [hep-ex]].

[27] ATLAS Collaboration, "Higgs Physics Public Results," https://twiki.cern.ch/twiki/bin/view/AtlasPublic/HiggsPublicResults

[28] CMS Collaboration, "Higgs Physics Public Results," https://twiki.cern.ch/twiki/bin/view/CMSPublic/PhysicsResultsHIG